ORIGINAL ARTICLE

A volume-fraction based algorithm for hybrid barotropic and non-barotropic two-fluid flow problems

Keh-Ming Shyue

Abstract The aim of this paper is to describe a simple Eulerian interface-capturing approach for the efficient numerical resolution of a hybrid barotropic and non-barotropic two-fluid flow problem in more than one space dimension. We use the compressible Euler equations as a model system with the thermodynamic property of each of the barotropic and non-barotropic fluid components characterized by the Tait and Noble–Abel equations of state, respectively. The algorithm is based on a volume fraction formulation of the equations together with an extended equation of state that is devised to give an approximate treatment for the mixture of more than one fluid component within a grid cell. A standard high-resolution wave propagation method is employed to solve the proposed two-fluid model with the dimensional-splitting technique incorporated in the method for multidimensional problems. Several numerical results are presented in one and two space dimensions that show the feasibility of the algorithm as applied to a reasonable class of practical problems without the occurrence of any spurious oscillation in the pressure near the smeared material interfaces. This includes, in particular, solutions for a study on the variation of the jet velocity with the incident shock pressure arising from the collapse of an air cavity in water under a shock wave.

Keywords Volume-fraction based algorithm · Tait equation of state · Noble–Abel equation of state · Gas-cavity collapse · Jetting

Communicated by K. Takayama.

K.-M. Shyue (✉)
Department of Mathematics, National Taiwan University,
Taipei 106, Taiwan
e-mail: shyue@math.ntu.edu.tw

1 Introduction

This paper is concerned with a simplified compressible two-phase flow problem where there is a material interface separating regions of two different barotropic and non-barotropic fluid components within an $N_d \geq 1$ spatial domain. In this problem, the flow regime of interest is assumed to be homogeneous with no jumps in the pressure and velocity (the normal component of it) across the interface, and the physical effects such as the viscosity, surface tension, and heat conduction are assumed to be small, and hence can be ignored in the problem formulation. With that, we use an Eulerian viewpoint of the model system, that on the barotropic part of the domain, the fluid is governed by the isentropic version of the compressible Euler equations as

$$\frac{\partial}{\partial t} \begin{bmatrix} \rho \\ \rho u_i \end{bmatrix} + \sum_{j=1}^{N_d} \frac{\partial}{\partial x_j} \begin{bmatrix} \rho u_j \\ \rho u_i u_j + p(\rho)\delta_{ij} \end{bmatrix} = 0, \qquad (1)$$

for $i = 1, 2, \ldots, N_d$, while on the non-barotropic part of the domain, the fluid is governed by the full set of the compressible Euler equations as

$$\frac{\partial}{\partial t} \begin{bmatrix} \rho \\ \rho u_i \\ \rho E \end{bmatrix} + \sum_{j=1}^{N_d} \frac{\partial}{\partial x_j} \begin{bmatrix} \rho u_j \\ \rho u_i u_j + p\delta_{ij} \\ \rho E u_j + p u_j \end{bmatrix} = 0. \qquad (2)$$

Here ρ, u_j, p, E, and δ_{ij} denote the density, the particle velocity in the x_j-direction, the pressure, the specific total energy, and the Kronecker delta, respectively.

To complete the model, in this work, the constitutive law for each of the barotropic and non-barotropic

components is taken to satisfy the Tait equation of state for compressible liquids (or called the Murnaghan equation of state in the context of an elastic solid [25]),

$$p(\rho) = (p_0 + \mathcal{B}) \left(\frac{\rho}{\rho_0} \right)^{\gamma} - \mathcal{B}, \tag{3}$$

and the Noble–Abel equation of state for real gases (or called the constant covolume equation of state [40]),

$$p(\rho, e) = \left(\frac{\gamma - 1}{1 - b\rho} \right) \rho e, \tag{4}$$

in a respective manner. Note that in the above expressions e represents the internal energy, ρ_0 and p_0 the density and pressure at a reference state, respectively, $\mathcal{B}$ a pressure-like constant, b a finite size of volume occupied by molecules ($0 \le b < 1/\rho$), and γ the adiabatic constant ($\gamma > 1$), see [20,23,27,45] for a typical set of data of practical importance. As usual, we have $E = e + \sum_{j=1}^{N_d} u_j^2/2$. Sample applications of this two-fluid model are, for instance, to the simulation of a shock-induced collapse of gas cavities in liquid [7,8] or to the simulation of an underwater explosion bubble [21,44].

For an efficient numerical resolution of this hybrid barotropic and non-barotropic two-fluid flow problem, we want to use a generalization of the classical shock-capturing method designed originally for single component flows in an Eulerian framework. It is known in the literature that the principal difficulty in the usual modification is the occurrence of spurious pressure oscillations when two or more fluid components are present in a grid cell. In the case of a barotropic or non-barotropic multicomponent problem, there has been quite a few numerical methods developed for that matter, see [1–3,9,14,15,26,31,43] and the references cited therein for more exposition. In the current interest of the problems consisting of separate barotropic and non-barotropic regions, there is, however, a relatively few attempts devoted to the subject, see [5,21,37] for an example using a somewhat complicated Lagrangian-type approach as compared to the current Eulerian one.

The basic approach we take here is an extension of the previous work advocated by the author [33,34,36] in that a mixture equation of state is introduced first as a basis to the modeling of the mixing between two different barotropic and non-barotropic fluid components. Then with the help of a volume-fraction function, we define an extended equation of state so that the pressure of the fluid can be determined explicitly no matter what fluid component (pure or not) is within a grid cell (see Sect. 2.1). Having that, as before, we are able to derive a volume-fraction based on the model system that consists of the full Euler equations for the basic conserved variables and an additional set of equations for the volume

fraction as well as the partial density of any one of the two fluid components in the problem. In our method, the latter equations are included in the algorithm primarily for an easy determination of the approximate location of the interface and also the computation of the pressure from the equation of state. It is important to note that these equations are put in a form so as to ensure a consistent modeling of the energy equation near the smeared interfaces and also the fulfillment of the mass equation in the other single component regions (see Sect. 2.2).

To find approximate solutions of our model system, we use a high-order Godunov method based on a wave-propagation formulation with the dimensional-splitting technique incorporated in the method for multidimensional problems. Numerical results to be presented in Sect. 4 show that this is a viable approach to a reasonable class of practical problems in one and two space dimensions, without producing any wrong oscillations in the pressure near the interfaces.

It should be emphasized that the methodology we have proposed here is by no means limited to the two-fluid flows with the above chosen equations of state. Extension of the algorithm to problems involving more than two fluid components and more complicated equations of state can be made in a straightforward manner by following the idea described in this paper and the five-equation model of Allaire et al. [3] and Massoni et al. [24]. Without going into the details for that, our goal is to establish the basic solution strategy and validate its use via some sample numerical experimentations.

The format of this paper is as follows. In Sect. 2, we describe the basic mathematical equations in a fluid-mixture form that will be used later in a numerical method for constructing approximate solutions of our model hybrid barotropic and non-barotropic two-fluid problems. In Sect. 3, we give a brief review of the HLLC approximate Riemann solver and the high-resolution wave-propagation methods for solving problems in one and more than one space dimensions. Numerical results of some sample examples are shown in Sect. 4.

2 Mathematical formulation

2.1 Equations of state

To start out, we want to build a mixture equation of state that is prerequisite in our approach for modeling the numerical mixing between the barotropic and non-barotropic fluid components within a grid cell. The first step, we take here, is to assume that thermodynamically the mixture of the fluids characterized by (3) and (4)

behaves like a typical non-barotropic fluid. Then using the first and second laws of thermodynamics, we may rewrite (3) and (4) in terms of the specific entropy S and the specific volume $V = 1/\rho$ as

$$p(V, S) = \mathcal{A}(\mathcal{S}) (p_0 + \mathcal{B}) \left(\frac{V_0}{V}\right)^\gamma - \mathcal{B}, \tag{5}$$

and

$$p(V, S) = \mathcal{A}(S) p_0 \left(\frac{V_0 - b}{V - b}\right)^\gamma, \tag{6}$$

for each in turn, where $\mathcal{A}(S) = \mathcal{R} \exp\left[(S - S_0)/C_V\right]$ (cf. [10]). Here C_V represents the specific heat at constant volume, $\mathcal{R}$ the universal gas constant, and S_0 the specific entropy at a reference state. As in the previous work for multicomponent problems with a van der Waals equation of state [33], we assume further that all the fluid components under concern is in an adiabatic equilibrium with the same entropy, and accordingly we propose to define an equation of state for the fluid mixture that combines (5) with (6) to be of the form

$$p(V, S) = \mathcal{A}(\mathcal{S}) (p_0 + \mathcal{B}) \left(\frac{V_0 - b}{V - b}\right)^\gamma - \mathcal{B}. \tag{7}$$

Notice that, with the use of this modified Noble–Abel equation of state (7), we recover not only the case (6) when $\mathcal{B} \to 0$, but also the case (5) and so (3) as we set $S = S_0$ in (5), when $b \to 0$. In the non-limiting case, however, where none of the material-dependent quantities $\mathcal{B}$ and b is close to zero, (7) does give a way to the representation of the cases in between, that is to the mixing of the present barotropic and non-barotropic components.

It should be mentioned that as a practical matter for many fluid flow problems away from cavitation (which is the situation studied here), rather than using (7) for the fundamental thermodynamic description of the fluid mixture, it is customary to formulate the equation in a way with the often-used variables in compressible hydrodynamics: ρ and e instead. Again, by employing the basic thermodynamic principles, this can be done quite easily, leading to

$$p(\rho, e) = \left(\frac{\gamma - 1}{1 - b\rho}\right) (\rho e - \mathcal{B}) - \mathcal{B}. \tag{8}$$

As to the computation of the fluid temperature T which is important in a wide variety of applications, we may use one of the formulas,

$$p(\rho, T) = \frac{\rho \mathcal{R} T}{1 - b\rho} - \mathcal{B},$$

$$e(\rho, T) = \frac{\mathcal{R} T}{\gamma - 1} + \frac{\mathcal{B}}{\rho},$$

for realization.

Now, for an easy identification of the type of fluid component within a grid cell, a volume-fraction function α is introduced here for that purpose. For example, when grid cells contain only the barotropic component we may set $\alpha = 1$, and so when grid cells contain only the non-barotropic component we set $\alpha = 0$. In case there are some cells cut by the interfaces where $\alpha \in (0, 1)$, we then have both of these components occupied by the volume fractions α and $1 - \alpha$ for each separately. With this definition of α, the pressure of our two-fluid flow problem in all the fluid-component scenarios within a grid cell can be determined straightforwardly by

$$p = \begin{cases} (p_0 + \mathcal{B}) \left(\frac{\rho}{\rho_0}\right)^\gamma - \mathcal{B} & \text{if } \alpha = 1 \\ \left(\frac{\gamma - 1}{1 - b\rho}\right) (\rho e - \mathcal{B}) - \mathcal{B} & \text{if } \alpha \neq 1, \end{cases} \tag{9}$$

provided all the variables appeared there are defined and known a priori. Finally, it should be remarked that in this work, the thermodynamical description of the materials of interest is limited by the stability requirement that the speed of sound of the fluid belongs to a set of real numbers.

2.2 Equations of motion

With the proposed constitutive law (9), it is clear that in regions where $\alpha = 0$ or $\alpha = 1$, there is no problem in using (1) and (2), respectively, for the complete description of the behavior of the underlying single-component flow. In regions where $\alpha \in (0, 1)$, as the fluid mixture is modeled in a non-barotropic manner, it is quite common to apply (2) as a model system that describes the motion of the mixtures of the basic conserved variables. Besides that, as in our previous work on numerical methods for compressible multicomponent problems (cf. [32,33,35,36]), we also bring in a set of effective equations for the problem-dependent material quantities so that the pressure can be computed easily from the equation of state.

2.2.1 γ-based effective equations

To derive the aforementioned effective equations for the mixture of material quantities in the current hybrid barotropic and non-barotropic flow application, we start with an interface-only problem as usual where both the pressure and each component of the particle velocities are constants in the domain, while the other variables such as the density and the material quantities are having jumps across some interfaces. Then, from (2), it is easy

to obtain equations for the time-dependent behavior of the density and total internal energy as

$$\frac{\partial \rho}{\partial t} + \sum_{j=1}^{N_d} u_j \frac{\partial \rho}{\partial x_j} = 0,$$

$$\frac{\partial}{\partial t}(\rho e) + \sum_{j=1}^{N_d} u_j \frac{\partial}{\partial x_j}(\rho e) = 0,$$

in a respective manner. Now, by inserting the modified Noble–Abel equation of state (8) into the latter one, we find an alternative description of the energy equation

$$\frac{\partial}{\partial t}\left(\frac{1-b\rho}{\gamma-1}p + \frac{\gamma-b\rho}{\gamma-1}\mathcal{B}\right)$$
$$+ \sum_{j=1}^{N_d} u_j \frac{\partial}{\partial x_j}\left(\frac{1-b\rho}{\gamma-1}p + \frac{\gamma-b\rho}{\gamma-1}\mathcal{B}\right) = 0 \qquad (10)$$

that is in relation to not only the pressure, but also the density and material quantities: γ, b, and $\mathcal{B}$.

In our algorithm, to maintain the pressure in equilibrium as it should be for this interface-only problem, we split (10) into the following two equations for the fluid mixtures $(1-b\rho)/(\gamma-1)$ and $(\gamma-b\rho)\mathcal{B}/(\gamma-1)$ as

$$\frac{\partial}{\partial t}\left(\frac{1-b\rho}{\gamma-1}\right) + \sum_{j=1}^{N_d} u_j \frac{\partial}{\partial x_j}\left(\frac{1-b\rho}{\gamma-1}\right) = 0, \qquad (11)$$

$$\frac{\partial}{\partial t}\left(\frac{\gamma-b\rho}{\gamma-1}\mathcal{B}\right) + \sum_{j=1}^{N_d} u_j \frac{\partial}{\partial x_j}\left(\frac{\gamma-b\rho}{\gamma-1}\mathcal{B}\right) = 0, \qquad (12)$$

respectively. We emphasize that in order to have the correct pressure equilibrium in (10), these are the two key equations that should be satisfied and approximated consistently (when the problem is solved numerically, see Sect. 3). On the other hand, as a practical matter, it is obvious that in addition to (11) and (12), we need to impose one more additional condition so as to have enough equations for the determination of all the three material quantities in (8). In our approach, see [33], this is done by simply breaking (11) into the following two parts:

$$\frac{\partial}{\partial t}\left(\frac{1}{\gamma-1}\right) + \sum_{j=1}^{N_d} u_j \frac{\partial}{\partial x_j}\left(\frac{1}{\gamma-1}\right) = 0, \qquad (13)$$

$$\frac{\partial}{\partial t}\left(\frac{b\rho}{\gamma-1}\right) + \sum_{j=1}^{N_d} u_j \frac{\partial}{\partial x_j}\left(\frac{b\rho}{\gamma-1}\right) = 0. \qquad (14)$$

Having done so, we arrive at a system of three equations (12)–(14) for the variables $(\gamma-b\rho)\mathcal{B}/(\gamma-1)$, $1/(\gamma-1)$, and $b\rho/(\gamma-1)$, in the order mentioned. Combining them to (2) yields a model system that is fundamental in

our algorithm for describing the behavior of the numerical mixing between the barotropic and non-barotropic components near the interface. With that, there is no difficulty to compute the pressure based on the equation of state,

$$p = \left[\rho E - \frac{\sum_{j=1}^{N_d}(\rho u_j)^2}{2\rho} - \frac{\gamma-b\rho}{\gamma-1}\mathcal{B}\right] \Big/ \left(\frac{1-b\rho}{\gamma-1}\right).$$

Up to this point, our discussion stresses only on an approach that is capable of keeping the pressure in equilibrium for a model interface-only problem. Since in practice we are interested in shock wave problems as well, we should take the equations, i.e., (12), (13), and (14), in a form such that γ, b, and $\mathcal{B}$ remain unchanged across both shocks and rarefaction waves. In this regard, it is known that with γ governed by (13), there is no problem to do so (cf. [1,32]). For b and $\mathcal{B}$, however, due to the appearance of the density term in (12) and (14), it turns out that in a time when such a situation occurs, for consistency with the mass conservation law of the fluid mixture they should be modified by

$$\frac{\partial}{\partial t}\left(\frac{\gamma-b\rho}{\gamma-1}\mathcal{B}\right) + \sum_{j=1}^{N_d} \frac{\partial}{\partial x_j}\left(\frac{\gamma-b\rho}{\gamma-1}\mathcal{B}u_j\right)$$
$$= \frac{\gamma\mathcal{B}}{\gamma-1}\sum_{j=1}^{N_d}\frac{\partial u_j}{\partial x_j}, \qquad (15)$$

and

$$\frac{\partial}{\partial t}\left(\frac{b\rho}{\gamma-1}\right) + \sum_{j=1}^{N_d} \frac{\partial}{\partial x_j}\left(\frac{b\rho}{\gamma-1}u_j\right) = 0, \qquad (16)$$

respectively, so that the mass-conserving property of the solution in the single component region can be acquired also (cf. [33]). We note that for convenience, we call the set of equations: (13), (15), and (16), a γ-based effective equations for the mixture of the material quantities of the modified Noble–Abel equation of state to be distinct from the other one presented below.

2.2.2 α-based effective equations

Before proceeding further, we comment that to find the initial fluid mixtures, $1/(\gamma-1)$, $(\gamma-b\rho)\mathcal{B}/(\gamma-1)$, and $b\rho/(\gamma-1)$, that is necessary when we initialize the data for multicomponent flow computations, we use the equation of state (8), where written as a function of the volume fraction α_ι, for $\iota = 1, 2$, and $\alpha_1 + \alpha_2 = 1$, it reads

$$\frac{1-b\rho}{\gamma-1}p + \frac{\gamma-b\rho}{\gamma-1}\mathcal{B} = \rho e = \sum_{\iota=1}^{2}\alpha_\iota\rho_\iota e_\iota$$

$$= \sum_{\iota=1}^{2}\alpha_\iota\left(\frac{1-b_\iota\rho_\iota}{\gamma_\iota-1}p_\iota + \frac{\gamma_\iota-b_\iota\rho_\iota}{\gamma_\iota-1}\mathcal{B}_\iota\right).$$

Here the subscript "ι" denotes the state variable of fluid component ι. By taking a similar approach as employed in Sect. 2.2.1 for the derivation of the γ-based effective equation it comes out readily as a splitting of the above expression into the relations:

$$\frac{1}{\gamma-1} = \sum_{\iota=1}^{2}\frac{\alpha_\iota}{\gamma_\iota-1}, \quad \frac{\gamma-b\rho}{\gamma-1}\mathcal{B} = \sum_{\iota=1}^{2}\alpha_\iota\frac{\gamma_\iota-b_\iota\rho_\iota}{\gamma_\iota-1}\mathcal{B}_\iota,$$

$$\frac{b\rho}{\gamma-1} = \sum_{\iota=1}^{2}\alpha_\iota\frac{b_\iota\rho_\iota}{\gamma_\iota-1}, \tag{17}$$

where in the process of splitting the terms the pressure p is chosen to fulfill the condition

$$\left(\frac{1-b\rho}{\gamma-1}\right)p = \sum_{\iota=1}^{2}\alpha_\iota\left(\frac{1-b_\iota\rho_\iota}{\gamma_\iota-1}\right)p_\iota. \tag{18}$$

Notice that when each of the partial pressures is in an equilibrium state within a grid cell, in conjunction with the first and third parts of (17), the pressure p obtained from (18) would remain in the same equilibrium as well, i.e., $p = p_\iota$, for $\iota = 1, 2$.

Now if the above volume-fraction notion of the states $1/(\gamma-1)$, $(\gamma-b\rho)\mathcal{B}/(\gamma-1)$, and $b\rho/(\gamma-1)$ are being employed in the γ-based effective equations, we are able to rewrite them straightforwardly into a componentwise form as

$$\frac{\partial}{\partial t}\left(\frac{\alpha_\iota}{\gamma_\iota-1}\right) + \sum_{j=1}^{N_d}u_j\frac{\partial}{\partial x_j}\left(\frac{\alpha_\iota}{\gamma_\iota-1}\right) = 0, \tag{19}$$

$$\frac{\partial}{\partial t}\left(\alpha_\iota\frac{\gamma_\iota-b_\iota\rho_\iota}{\gamma_\iota-1}\mathcal{B}_\iota\right) + \sum_{j=1}^{N_d}\frac{\partial}{\partial x_j}\left(\alpha_\iota\frac{\gamma_\iota-b_\iota\rho_\iota}{\gamma_\iota-1}\mathcal{B}_\iota u_j\right)$$

$$= \alpha_\iota\frac{\gamma_\iota\mathcal{B}_\iota}{\gamma_\iota-1}\sum_{j=1}^{N_d}\frac{\partial u_j}{\partial x_j}, \tag{20}$$

$$\frac{\partial}{\partial t}\left(\alpha_\iota\frac{b_\iota\rho_\iota}{\gamma_\iota-1}\right) + \sum_{j=1}^{N_d}\frac{\partial}{\partial x_j}\left(\alpha_\iota\frac{b_\iota\rho_\iota}{\gamma_\iota-1}u_j\right) = 0, \tag{21}$$

for $\iota = 1, 2$. Then based on the fact that all the material quantities γ_ι, b_ι, and $\mathcal{B}_\iota$ will be kept as a constant in each phase of the domain at all time, from (19), it is easy to find the transport equation for the volume fraction α_ι as

$$\frac{\partial\alpha_\iota}{\partial t} + \sum_{j=1}^{N_d}u_j\frac{\partial\alpha_\iota}{\partial x_j} = 0, \tag{22}$$

whereas from (21), we find the mass conservation law for the fluid component ι as

$$\frac{\partial}{\partial t}(\rho_\iota\alpha_\iota) + \sum_{j=1}^{N_d}\frac{\partial}{\partial x_j}(\rho_\iota\alpha_\iota u_j) = 0. \tag{23}$$

Furthermore, in the case of (20), after some simple algebraic manipulations, it can be expressed by the form

$$\frac{\gamma_\iota\mathcal{B}_\iota}{\gamma_\iota-1}\left[\frac{\partial\alpha_\iota}{\partial t} + \sum_{j=1}^{N_d}u_j\frac{\partial\alpha_\iota}{\partial x_j}\right]$$

$$-\frac{b_\iota\mathcal{B}_\iota}{\gamma_\iota-1}\left[\frac{\partial}{\partial t}(\rho_\iota\alpha_\iota) + \sum_{j=1}^{N_d}\frac{\partial}{\partial x_j}(\rho_\iota\alpha_\iota u_j)\right] = 0,$$

yielding naturally the same set of governing equations as before, i.e., (22) and (23). It is apparent that if the solutions of α_ι and $\rho_\iota\alpha_\iota$ are known from the equations, we may therefore compute $1/(\gamma-1)$, $(\gamma-b\rho)\mathcal{B}/(\gamma-1)$, and $b\rho/(\gamma-1)$ directly according to (17). Thus, instead of using the γ-based effective equations, it is a viable alternate to use the α-based equations: (22) and (23), for the motion of the mixture of the material quantities of the problem.

2.2.3 Complete model system

It is important to mention that to make up a complete model system that is capable of dealing with all the fluid component cases, $\alpha = 1$ (barotropic phase), $\alpha = 0$ (non-barotropic phase), or $\alpha \in (0, 1)$ (barotropic and non-barotropic coexistence phase), we have to know the approximate location of the interfaces so that the correct equations of motion as well as the equation of state can be employed to each part of the domain, from the current time to the next. Here, as $\alpha_1 + \alpha_2 = 1$, it is clear that if we choose $\alpha_1 = \alpha$ and so $\alpha_2 = 1 - \alpha$, the two transport equations in (22) for each of α_1 and α_2 can be combined, without affecting anything, to a single one for α as

$$\frac{\partial\alpha}{\partial t} + \sum_{j=1}^{N_d}u_j\frac{\partial\alpha}{\partial x_j} = 0, \tag{24}$$

leading to the evolution equation we use in the algorithm for that matter. Note that, in devising a fluid-mixture type algorithm for multicomponent problems, one common practice is to consider the mixture of the total density, $\rho = \rho_1\alpha_1 + \rho_2\alpha_2$, as one of the basic variables in the proposed model system (cf. [32,33,35]). When this

is the case, it should be more sensible to include only one of the equations in (23) together with the last two relations in (17) than the use of both (15) and (16) for the variables $(\gamma - b\rho)\mathcal{B}/(\gamma - 1)$ and $b\rho/(\gamma - 1)$.

Putting all things together, with the equation of state (9), the model equations with which we propose to solve the present two-fluid flow problems in more than one space dimension take the form

$$\frac{\partial \rho}{\partial t} + \sum_{j=1}^{N_d} \frac{\partial}{\partial x_j}\left(\rho u_j\right) = 0$$

$$\frac{\partial}{\partial t}(\rho u_i) + \sum_{j=1}^{N_d} \frac{\partial}{\partial x_j}(\rho u_i u_j + p\delta_{ij}) = 0$$

$$\frac{\partial}{\partial t}(\rho E) + \sum_{j=1}^{N_d} \frac{\partial}{\partial x_j}\left(\rho E u_j + p u_j\right) = 0 \quad \text{if} \quad \alpha \neq 1, \quad (25)$$

$$\frac{\partial}{\partial t}(\rho_1 \alpha) + \sum_{j=1}^{N_d} \frac{\partial}{\partial x_j}\left(\rho_1 \alpha u_j\right) = 0$$

$$\frac{\partial \alpha}{\partial t} + \sum_{j=1}^{N_d} u_j \frac{\partial \alpha}{\partial x_j} = 0$$

for $i = 1, 2, \ldots, N_d$. Note that when $\alpha \neq 1$ we have a system of $N_d + 4$ equations for the motion of both the pure non-barotropic phase and the fluid mixture. Clearly, the first $N_d + 2$ of them are simply the basic conservation of the mass, momenta (N_d of them), and total energy, while the last two equations are (23) and (24) that are used to find the variables $1/(\gamma - 1)$, $(\gamma - b\rho)\mathcal{B}/(\gamma - 1)$, and $b\rho/(\gamma - 1)$ from the relations in (17), and also the approximate location of the interface (the volume fraction function α does it). On the other instance, when $\alpha = 1$, we just have the first $N_d + 1$ equations governing the single-component barotropic flow as usual. With a system expressing in this way, there is no problem to compute all the state variables of interest, including the pressure from the equation of state. The initialization of the state variables in (25) for fluid-mixture cells can be made in a standard way as described in [32,33] for numerical simulations.

It should be remarked that for an easy extension of the proposed model to more complex equations of state we have taken (25) in a form that is analogous to the five-equation model advocated by Allaire et al. [3] or Massoni et al. [24] for compressible multicomponent flow problems with general non-barotropic equation of state. For any given N_d, if the state variables of the flow are all in the region of the thermodynamic stability (this is the case we are interested in here), it is not difficult to show that (25) is a hyperbolic system in the sense that any

linear combination of the matrices A_j, $j = 1, 2, \ldots, N_d$, appearing in the quasi-linear form of the equations

$$\frac{\partial q}{\partial t} + \sum_{j=1}^{N_d} A_j(q) \frac{\partial q}{\partial x_j} = 0 \qquad (26)$$

has real eigenvalues and a complete set of eigenvectors.

As an example, we consider the three-dimensional case $N_d = 3$, and then have the state vector q in (26) defined by

$$q = (\rho, \ \rho u_1, \ \rho u_2, \ \rho u_3, \ \rho E, \ \rho_1 \alpha, \ \alpha)^T,$$

and the matrices A_j, for $j = 1, 2, 3$, defined by

$$A_1 = \begin{bmatrix} 0 & 1 & 0 & 0 & 0 & 0 & 0 \\ K - u_1^2 & 2u_1 + \eta_2 & \eta_3 & \eta_4 & \Gamma & \varphi & \chi \\ -u_1 u_2 & u_2 & u_1 & 0 & 0 & 0 & 0 \\ -u_1 u_3 & u_3 & 0 & u_1 & 0 & 0 & 0 \\ u_1(K - H) & H + u_1\eta_2 & u_1\eta_3 & u_1\eta_4 & u_1(\Gamma + 1) & u_1\varphi & u_1\chi \\ -u_1\rho_1\alpha/\rho & \rho_1\alpha/\rho & 0 & 0 & 0 & u_1 & 0 \\ 0 & 0 & 0 & 0 & 0 & 0 & u_1 \end{bmatrix},$$

$$A_2 = \begin{bmatrix} 0 & 0 & 1 & 0 & 0 & 0 & 0 \\ -u_1 u_2 & u_2 & u_1 & 0 & 0 & 0 & 0 \\ K - u_2^2 & \eta_2 & 2u_2 + \eta_3 & \eta 4 & \Gamma & \varphi & \chi \\ -u_2 u_3 & 0 & u_3 & u_2 & 0 & 0 & 0 \\ u_2(K - H) & u_2\eta_2 & H + u_2\eta_3 & u_2\eta_4 & u_2(\Gamma + 1) & u_2\varphi & u_2\chi \\ -u_2\rho_1\alpha/\rho & 0 & \rho_1\alpha/\rho & 0 & 0 & u_2 & 0 \\ 0 & 0 & 0 & 0 & 0 & 0 & u_2 \end{bmatrix},$$

$$A_3 = \begin{bmatrix} 0 & 0 & 0 & 1 & 0 & 0 & 0 \\ -u_1 u_3 & u_3 & 0 & u_1 & 0 & 0 & 0 \\ -u_2 u_3 & 0 & u_3 & u_2 & 0 & 0 & 0 \\ K - u_3^2 & \eta_2 & \eta_3 & 2u_3 + \eta_4 & \Gamma & \varphi & \chi \\ u_3(K - H) & u_3\eta_2 & u_3\eta_3 & H + u_3\eta_4 & u_3(\Gamma + 1) & u_3\varphi & u_3\chi \\ -u_3\rho_1\alpha/\rho & 0 & 0 & \rho_1\alpha/\rho & 0 & u_3 & 0 \\ 0 & 0 & 0 & 0 & 0 & 0 & u_3 \end{bmatrix}.$$

With that, the eigenvalues and the corresponding eigenvectors of the matrices are:
for matrix A_1:

$$\Lambda_{A_1} = \text{diag}\left(\lambda_1^{(1)}, \lambda_2^{(1)}, \ldots, \lambda_7^{(1)}\right)$$
$$= \text{diag}(u_1 - c, \ u_1, \ u_1 + c, \ u_1, \ \ldots, \ u_1),$$
$$R_{A_1} = \left(r_1^{(1)}, r_2^{(1)}, \ldots, r_7^{(1)}\right)$$
$$= \begin{bmatrix} 1 & 1 & 1 & 0 & 0 & 0 & 0 \\ u_1 - c & u_1 & u_1 + c & 0 & 0 & 0 & 0 \\ u_2 & u_2 & u_2 & 1 & 0 & 0 & 0 \\ u_3 & u_3 & u_3 & 0 & 1 & 0 & 0 \\ H - u_1 c & K/\Gamma & H + u_1 c & u_2 & u_3 & -\varphi/\Gamma & -\chi/\Gamma \\ \rho_1\alpha/\rho & 0 & \rho_1\alpha/\rho & 0 & 0 & 1 & 0 \\ 0 & 0 & 0 & 0 & 0 & 0 & 1 \end{bmatrix},$$

for matrix A_2:

$$\Lambda_{A_2} = \text{diag}\left(\lambda_1^{(2)}, \lambda_2^{(2)}, \ldots, \lambda_7^{(2)}\right)$$
$$= \text{diag}(u_2 - c, u_2, u_2 + c, u_2, \ldots, u_2),$$
$$R_{A_2} = \left(r_1^{(2)}, r_2^{(2)}, \ldots, r_7^{(2)}\right)$$

$$= \begin{bmatrix}
1 & 1 & 1 & 0 & 0 & 0 & 0 \\
u_1 & u_1 & u_1 & 1 & 0 & 0 & 0 \\
u_2 - c & u_2 & u_2 + c & 0 & 0 & 0 & 0 \\
u_3 & u_3 & u_3 & 0 & 1 & 0 & 0 \\
H - u_2 c & K/\Gamma & H + u_2 c & u_1 & u_3 & -\varphi/\Gamma & -\chi/\Gamma \\
\rho_1 \alpha/\rho & 0 & \rho_1 \alpha/\rho & 0 & 0 & 1 & 0 \\
0 & 0 & 0 & 0 & 0 & 0 & 1
\end{bmatrix},$$

and
for matrix A_3:

$$\Lambda_{A_3} = \text{diag}\left(\lambda_1^{(3)}, \lambda_2^{(3)}, \ldots, \lambda_7^{(3)}\right)$$
$$= \text{diag}(u_3 - c, u_3, u_3 + c, u_3, \ldots, u_3),$$
$$R_{A_3} = \left(r_1^{(3)}, r_2^{(3)}, \ldots, r_7^{(3)}\right)$$

$$= \begin{bmatrix}
1 & 1 & 1 & 0 & 0 & 0 & 0 \\
u_1 & u_1 & u_1 & 1 & 0 & 0 & 0 \\
u_2 & u_2 & u_2 & 0 & 1 & 0 & 0 \\
u_3 - c & u_3 & u_3 + c & 0 & 0 & 0 & 0 \\
H - u_3 c & K/\Gamma & H + u_3 c & u_1 & u_2 & -\varphi/\Gamma & -\chi/\Gamma \\
\rho_1 \alpha/\rho & 0 & \rho_1 \alpha/\rho & 0 & 0 & 1 & 0 \\
0 & 0 & 0 & 0 & 0 & 0 & 1
\end{bmatrix};$$

$A_j r_k^{(j)} = \lambda_k^{(j)} r_k^{(j)}$, $j = 1, 2, 3$, and $k = 1, 2, \ldots, 7$. Here $c = \sqrt{[\gamma/(1 - b\rho)][(p + \mathcal{B})/\rho]}$ is the speed of sound of the fluid, and the other notations appeared in the above formulae are set by $\Gamma = (\gamma - 1)/(1 - b\rho)$, $K = (\Gamma \sum_{j=1}^3 u_j^2/2) + \zeta$, $H = E + p/\rho$, $\eta_i = -u_i \Gamma$, for $i = 1, 2, 3$, $\varphi = \Gamma\Delta[b\mathcal{B}/(\gamma - 1)] - p\Delta[b/(\gamma - 1)]/\Gamma$, and $\chi = -\Gamma\Delta[\gamma\mathcal{B}/(\gamma - 1)] + p\Delta[1/(\gamma - 1)]/\Gamma$, where $\zeta = -b_2/(\gamma_2 - 1)[(\Gamma\mathcal{B}_2) + (p/\Gamma)]$ and $\Delta[\kappa] = \kappa_1 - \kappa_2$.

It should be noted that since the volume fraction function α is governed by a linear transport equation of the form (24) and its solution can only have jumps across the material interfaces, but not across other waves such as shock and rarefaction, we easily find the usual expression of the Rankine–Hugoniot jump conditions across shock waves for this two-fluid model (25) (cf. [33]). Finally, for the ease of the latter reference, it is customary to write (25) into a more compact expression by

$$\frac{\partial q}{\partial t} + \sum_{j=1}^{N_d} f_j\left(\frac{\partial}{\partial x_j}, q\right) = 0, \tag{27}$$

where f_j is taken as the vector-value function of the form

$$f_j = \left[\frac{\partial}{\partial x_j}(\rho u_j), \frac{\partial}{\partial x_j}(\rho u_1 u_j + p\delta_{1j}), \ldots, \frac{\partial}{\partial x_j}(\rho u_{N_d} u_j \right.$$
$$\left. + p\delta_{N_d j}), \frac{\partial}{\partial x_j}(\rho E u_j + p u_j), \frac{\partial}{\partial x_j}(\rho_1 \alpha u_j), u_j \frac{\partial \alpha}{\partial x_j}\right]^{\text{T}},$$

for $j = 1, 2, \ldots, N_d$.

3 Numerical approximations

To find approximate solutions of our two-fluid model presented in Sect. 2, we use a standard high-resolution wave propagation method developed by LeVeque [17, 18] for general hyperbolic systems of partial differential equations. This method is a different form of the fluctuation-and-signal scheme of Roe [29,30] in that we solve one-dimensional Riemann problems at each cell interface, and use the resulting waves (i.e., discontinuities moving at constant speeds) to update the solutions in neighboring grid cells. To achieve second-order accurate on smooth solutions, and sharp and monotone profiles on discontinuous solutions, we introduce slopes and limiters to the method as in many other high-resolution schemes for conservation laws [11,19,39].

3.1 HLL-type approximate Riemann solvers

As a preliminary, we begin by reviewing the construction of the approximate Riemann problem solutions in one space dimension which is one of the major elements in our numerical algorithm. If we consider the case $N_d = 3$ as an example, to simplify the notation, rather than using x_j for the spatial variable and u_j for the particle velocity, for $j = 1, 2, 3$, we take the often-employed symbols (x, y, z) and (u, v, w) for that matter instead. Then the problem to be solved is to find the solution of (25) in the direction normal to one of the xy, yz, and xz planes, with piecewise constant data q_L and q_R to the left and right of the cell interface. It should be noted that in the applications concerned here, we have chosen the data q_L and q_R well enough so that the solution of the Riemann problem would consist of genuinely non-linear waves such as shock and rarefaction, and linearly degenerate wave such as contact discontinuity; there is no vacuum region occurring in the solution. Without loss of generality, in the following we only look at the Riemann problem in the direction normal to the yz plane.

There are a wide variety of approaches proposed in the literature for determining an approximate solution of the Riemann problem, see [41], for example. Here we are interested in a simple variant of the Riemann solver

based on the work of Harten et al. [13] for hyperbolic systems of conservation laws,

$$\frac{\partial q}{\partial t} + \frac{\partial}{\partial x} f(q) = 0, \tag{28}$$

where $q \in \mathbb{R}^n$ is the vector of conserved variables for a system of n equations and f the flux function. Recall that in the original version of the HLL solver, the solution of the Riemann problem is assumed to be composed of two discontinuities propagating at constant speeds λ_L and λ_R to the left and right, $\lambda_\mathrm{L} \neq \lambda_\mathrm{R}$, separating three constant states in the space-time domain. If we assume further that λ_L and λ_R are known a priori by some simple estimates based on the local information of the wave speeds, then by using the integral form of the conservation laws over a sufficiently large control volume $[-M, M] \times [0, T]$, for some positive M and $T \in \mathbb{R}$, it is easy to find the constant state in the middle region, denoted by q_m, as the average of the exact solution over the interval $[\lambda_\mathrm{L} T, \lambda_\mathrm{R} T]$ at time T,

$$\begin{aligned} q_\mathrm{m} &= \frac{1}{(\lambda_\mathrm{R} - \lambda_\mathrm{L}) T} \int\limits_{\lambda_\mathrm{L} T}^{\lambda_\mathrm{R} T} q(x, T) \, \mathrm{d}x \\ &= \frac{\lambda_\mathrm{R} q_\mathrm{R} - \lambda_\mathrm{L} q_\mathrm{L} - f(q_\mathrm{R}) + f(q_\mathrm{L})}{\lambda_\mathrm{R} - \lambda_\mathrm{L}}, \end{aligned} \tag{29}$$

where $f(q_\iota)$ is the flux evaluated at the state q_ι, for $\iota = \mathrm{L}$ or R.

In spite of the fact that the above 2-wave HLL solver has been applied quite successfully to many numerical methods for solving problems governed by (28), it is known, however, that the numerical result obtained by using this solver is too diffusive for contact discontinuities. In addition to that, because of the lack of information on the structure of the material interfaces, it is not feasible at all to the more general multicomponent problems like the one considered in this article. Nevertheless, as recommended by Toro et al. [6,42], this 2-wave Riemann solver can be improved quite easily by introducing an additional middle wave of speed u_m in the solution structure for modeling the speed of contact discontinuity, yielding a 3-wave HLL (or called HLLC) solver. Note that if we have had the first two components of q_m computed from (29), we may simply set $u_\mathrm{m} = q_\mathrm{m}^{(2)}/q_\mathrm{m}^{(1)}$ (cf. [31,36]), where $q_\mathrm{m}^{(i)}$ is the ith component of the vector q_m, see [41] for the various other possible choices.

With that, our goal next is to find the constant states q_mL and q_mR in the regions m_L and m_R to the left and right of the middle wave, respectively. We do this by making use of the integral form of the conservation laws again, but now applied over a control volume $[-M, u_\mathrm{m} T - \epsilon] \times [0, T]$ for the state q_mL, and over a

control volume $[u_\mathrm{m} T + \epsilon, M] \times [0, T]$ for the state q_mR, $0 < \epsilon \ll 1$. When the aforementioned procedure is taken effect to the current two-fluid model (25) in the prescribed direction, it is not difficult to show that the result is

$$q_{\mathrm{m}\iota}^{(1)} = \frac{f_{\mathrm{m}\iota}^{(1)}}{\lambda_\iota - u_\mathrm{m}}, \quad q_{\mathrm{m}\iota}^{(2)} = u_\mathrm{m} q_{\mathrm{m}\iota}^{(1)}, \quad q_{\mathrm{m}\iota}^{(3)} = v_\iota q_{\mathrm{m}\iota}^{(1)},$$

$$q_{\mathrm{m}\iota}^{(4)} = w_\iota q_{\mathrm{m}\iota}^{(1)}, \quad q_{\mathrm{m}\iota}^{(5)} = \frac{f_{\mathrm{m}\iota}^{(5)} + u_\mathrm{m} \left(u_\mathrm{m} f_{\mathrm{m}\iota}^{(1)} - f_{\mathrm{m}\iota}^{(2)} \right)}{\lambda_\iota - u_\mathrm{m}}, \tag{30}$$

$$q_{\mathrm{m}\iota}^{(6)} = \frac{f_{\mathrm{m}\iota}^{(6)}}{\lambda_\iota - u_\mathrm{m}}, \quad q_{\mathrm{m}\iota}^{(7)} = q_\iota^{(7)},$$

where $f_{\mathrm{m}\iota}^{(i)} = \lambda_\iota q_\iota^{(i)} - f^{(i)}(q_\iota)$ represents the ith component of the vector $f_{\mathrm{m}\iota}$, for $\iota = \mathrm{L}$ or R. It is interesting to remark that $q_{\mathrm{mL}}^{(i)}$ and $q_{\mathrm{mR}}^{(i)}$ satisfy the basic consistency condition of the integral form of the conservation laws,

$$\left(\frac{u_\mathrm{m} - \lambda_\mathrm{L}}{\lambda_\mathrm{R} - \lambda_\mathrm{L}} \right) q_{\mathrm{Lm}}^{(i)} + \left(\frac{\lambda_\mathrm{R} - u_\mathrm{m}}{\lambda_\mathrm{R} - \lambda_\mathrm{L}} \right) q_{\mathrm{mR}}^{(i)} = q_\mathrm{m}^{(i)},$$

for $i = 1, 2, \ldots, 6$. By taking $\lambda_\mathrm{L} = \min(u_\mathrm{L} - c_\mathrm{L}, u_\mathrm{R} - c_\mathrm{R})$ and $\lambda_\mathrm{R} = \max(u_\mathrm{L} + c_\mathrm{L}, u_\mathrm{L} + c_\mathrm{L})$, for instance, we may then set the speed of the three moving discontinuities by $\lambda_1 = \lambda_\mathrm{L}$, $\lambda_2 = u_\mathrm{m}$, $\lambda_3 = \lambda_\mathrm{R}$, and the jumps across each of them by

$$\mathcal{W}_1 = q_\mathrm{mL} - q_\mathrm{L}, \quad \mathcal{W}_2 = q_\mathrm{mR} - q_\mathrm{mL}, \quad \mathcal{W}_3 = q_\mathrm{R} - q_\mathrm{mR},$$

using the result (30). As usual, wave propagation methods (to be described below) are based on using these propagating discontinuity to update the cell averages in the cells neighboring each interface.

3.2 Wave propagation methods

3.2.1 One-dimensional case

To review the basic idea of our underlying integration scheme, it is instructive to look at the simplest $N_\mathrm{d} = 1$ case of our model system,

$$\frac{\partial q}{\partial t} + f_1 \left(\frac{\partial}{\partial x}, q \right) = 0,$$

with q and f_1 defined as in (25) and (27). For simplicity, we describe the method on a uniform grid with fixed mesh spacing Δx in the x-direction, and use a standard finite-volume formulation in which the discretized solution Q_j^n approximates the cell average over the grid cell $[x_j, x_{j+1}]$ at time t_n,

$$Q_j^n \approx \frac{1}{\Delta x} \int\limits_{x_j}^{x_{j+1}} q(x, t_n) \, \mathrm{d}x.$$

The time step from the current time t_n to the next t_{n+1} is denoted by Δt.

In this numerical setup, a first order accurate version of the method in wave-propagation form is a Godunov-type scheme that can be written as

$$Q_j^{n+1} = Q_j^n - \frac{\Delta t}{\Delta x} \sum_{m=1}^{m_{\mathrm{w}}} \left(\lambda_m^- \mathcal{W}_m \right)_{j+1}^n + \left(\lambda_m^+ \mathcal{W}_m \right)_j^n. \qquad (31)$$

Here λ_m and $\mathcal{W}_m$ are solutions of the mth wave family, for $m = 1, 2, \ldots, m_{\mathrm{w}}$, obtained from solving the Riemann problems at cell interfaces x_j and x_{j+1} with a properly chosen solver, and $\lambda^- = \min(\lambda, 0)$, $\lambda^+ = \max(\lambda, 0)$. It is known that method (31) belongs to a class of upwind schemes and is stable when the typical CFL (Courant–Friedrichs–Lewy) condition is satisfied (cf. [11,19]). Moreover, it is not difficult to show that the method is quasi-conservative in the sense that when applying the method to (25) not only the conservation laws but also the transport equation is approximated in a consistent manner by the method, see [33] for the details.

To improve the accuracy of (31) to high resolution, it is a standard approach by first introducing correction waves in a piecewise-linear form with zero mean value, and then propagating each wave over the time step Δt to update the cell averages it overlaps. Without providing the details in this place (cf. [19] for example), with the corrections, (31) is modified by

$$Q_j^{n+1} := Q_j^{n+1} - \frac{1}{2} \sum_{m=1}^{m_{\mathrm{w}}} \left(|\mu_m| \left(1 - |\mu_m| \right) \widetilde{\mathcal{W}}_m \right)_{j+1}^n$$
$$- \left(|\mu_m| \left(1 - |\mu_m| \right) \widetilde{\mathcal{W}}_m \right)_j^n, \qquad (32)$$

where $\mu_m = \lambda_m \Delta t / \Delta x$, and $\widetilde{\mathcal{W}}_m$ is a limited value of $\mathcal{W}_m$ obtained by comparing $\mathcal{W}_m$ with the corresponding $\mathcal{W}_m$ from the neighboring Riemann problem to the left (if $\lambda_m > 0$) or to the right (if $\lambda_m < 0$).

Note that when utilizing the wave-form representation of the Riemann problem solution, it is common practice to perform the limiting procedure over each component of the wave via a limiter function Φ (eg, by using the minmod function $\Phi(\theta) = \max(0, \min(1, \theta))$ or some others as discussed in [39]), and set

$$\widetilde{\mathcal{W}}_{mj}^{(i)} = \Phi\left(\theta_{mj}^{(i)} \right) \mathcal{W}_{mj}^{(i)} \quad \text{with} \quad \theta_{mj}^{(i)} = \frac{\mathcal{W}_{mJ}^{(i)}}{\mathcal{W}_{mj}^{(i)}},$$

$$J = \begin{cases} j - 1 & \text{if } \lambda_{mj} \geq 0 \\ j + 1 & \text{if } \lambda_{mj} < 0 \end{cases}, \qquad (33)$$

where $\mathcal{W}_{mj}^{(i)}$ is the ith component of $\mathcal{W}_{mj}$. While the above approach works in a satisfactory manner for many single component problems, it was shown in [36] that,

for general multicomponent problems, to ensure a consistent approximation of the total energy near the interfaces the third limited component of the 2-wave, $\widetilde{\mathcal{W}}_{2j}^{(3)}$, should be modified so that the desired pressure equilibrium can be maintained there.

Having this in mind, following the previous work done in [36], we make a new definition of $\widetilde{\mathcal{W}}_{2j}^{(3)}$ as

$$\widetilde{\mathcal{W}}_{2j}^{(3)} := \Phi\left(\frac{\bar{\mathcal{W}}_{2J}}{\bar{\mathcal{W}}_{2j}} \right) \bar{\mathcal{W}}_{2j} - \Delta \left[\frac{b\mathcal{B}}{\gamma - 1} \right] \widetilde{\mathcal{W}}_{2j}^{(4)}$$
$$+ \Delta \left[\frac{\gamma \mathcal{B}}{\gamma - 1} \right] \widetilde{\mathcal{W}}_{2j}^{(5)},$$

where $\bar{\mathcal{W}}_{2\iota} = \mathcal{W}_{2\iota}^{(3)} + \Delta[b\mathcal{B}/(\gamma - 1)]\mathcal{W}_{2\iota}^{(4)} - \Delta[\gamma\mathcal{B}/(\gamma - 1)]\mathcal{W}_{2\iota}^{(5)}$, for $\iota = j$ and J (ie, $j - 1$ or $j + 1$ depending on the propagating direction of λ_{2j}); $\Delta[\kappa] = \kappa_1 - \kappa_2$. With this revision of the limited 2-wave on the total energy, it is not difficult to show that for a model interface-only problem (see Sect. 2.2) we again have the required pressure equilibrium without introducing any spurious oscillations in the approximate solution. Besides that we would typically obtain a better resolution of the result as compared to the first order result, see [36] for details.

3.2.2 Multidimensional case

To extend the one-dimensional wave propagation method to more space dimensions, here we take a simple dimensional-splitting approach in which a multidimensional problem is split into a sequence of one-dimensional problems. Consider the three-dimensional case $N_{\mathrm{d}} = 3$, for example. The hybrid barotropic and non-barotropic two-fluid flow problem modeled by (27), i.e.,

$$\frac{\partial q}{\partial t} + f_1\left(\frac{\partial}{\partial x}, q \right) + f_2\left(\frac{\partial}{\partial y}, q \right) + f_3\left(\frac{\partial}{\partial z}, q \right) = 0,$$

can be split into

$$x\text{-sweeps:} \quad \frac{\partial q}{\partial t} + f_1\left(\frac{\partial}{\partial x}, q \right) = 0, \qquad (34a)$$

$$y\text{-sweeps:} \quad \frac{\partial q}{\partial t} + f_2\left(\frac{\partial}{\partial y}, q \right) = 0, \qquad (34b)$$

$$z\text{-sweeps:} \quad \frac{\partial q}{\partial t} + f_3\left(\frac{\partial}{\partial z}, q \right) = 0. \qquad (34c)$$

Assume a uniform Cartesian grid with fixed mesh spacing Δx, Δy, and Δz in the x-, y-, and z-direction, respectively. In a finite-volume formulation of the solution, the value Q_{ijk}^n would approximate the cell average of the solution over the (i, j, k)th grid cell at time t_n,

$$Q_{ijk}^n \approx \frac{1}{\Delta x \Delta y \Delta z} \int\int\int_{\mathcal{C}_{ijk}} q(x, y, z, t_n) \, dx \, dy \, dz,$$

where $\mathcal{C}_{ijk} = [x_i, x_{i+1}] \times [y_j, y_{j+1}] \times [z_k, z_{k+1}]$ denotes the cubical region occupied by the grid cell (i, j, k). Then a dimensional-splitting (or called Godunov-splitting) version of the first-order wave propagation method in three dimensions can be written as

$$Q_{ijk}^* = Q_{ijk}^n - \frac{\Delta t}{\Delta x} \sum_{m=1}^{m_w} \left(\lambda_m^{(1)-} \mathcal{W}_m^{(1)} \right)_{i+1,jk}^n$$
$$+ \left(\lambda_m^{(1)+} \mathcal{W}_m^{(1)} \right)_{ijk}^n, \tag{35a}$$

$$Q_{ijk}^{**} = Q_{ijk}^* - \frac{\Delta t}{\Delta y} \sum_{m=1}^{m_w} \left(\lambda_m^{(2)-} \mathcal{W}_m^{(2)} \right)_{i,j+1,k}^*$$
$$+ \left(\lambda_m^{(2)+} \mathcal{W}_m^{(2)} \right)_{ijk}^*, \tag{35b}$$

$$Q_{ijk}^{n+1} = Q_{ijk}^{**} - \frac{\Delta t}{\Delta z} \sum_{m=1}^{m_w} \left(\lambda_m^{(3)-} \mathcal{W}_m^{(3)} \right)_{ij,k+1}^{**}$$
$$+ \left(\lambda_m^{(3)+} \mathcal{W}_m^{(3)} \right)_{ijk}^{**}. \tag{35c}$$

Note that in the x-sweeps we start with cell average Q_{ijk}^n at time t_n and solve (34a) along each row of cells $\mathcal{C}_{ijk}$ with j and k fixed, updating Q_{ijk}^n to Q_{ijk}^* by the use of (35a), where $\lambda_{m,ijk}^{(1)}$ and $\mathcal{W}_{m,ijk}^{(1)}$ are solutions of the mth wave family obtained from solving the one-dimensional Riemann problems in the direction normal to the cell interface between $\mathcal{C}_{ijk}$ and $\mathcal{C}_{i+1,jk}$ with Q_{ijk}^n and $Q_{i+1,jk}^n$ as initial data. Consequently in the y-sweeps we can use the Q_{ijk}^* values as data for solving (34b) along each column of cells $\mathcal{C}_{ijk}$ with i and k fixed, which gives us Q_{ijk}^{**} from (35b). Finally, in the z-sweeps we use the Q_{ijk}^{**} values as data for solving (34c) along the other column of cells $\mathcal{C}_{ijk}$ with i and j fixed, yielding the solution of the next time step Q_{ijk}^{n+1} from (35c). Clearly, in each one-dimensional sweep, one may apply the same high-resolution approach as before to improve numerical accuracy of this splitting method.

It is a known fact that, except for some simple problems, there will be generally splitting error of the method just described. But from numerical experiences it turns out that the splitting error is often no worse than the errors introduced by the numerical methods in each sweep, and hence as a practical matter it is typically not necessary to use a more accurate splitting approach such as the Strang splitting [38] to reduce the splitting error, see [19] for some discussion of why one might not want to use a higher order splitting method. In addition, we have also observed good results for many practical

problems obtained using the present method as compared to the fully discrete wave propagation method (cf. [16–18]). For these reasons, we will use the one-dimensional high-resolution wave propagation method together with the Godunov splitting for all the multidimensional tests done in the next section.

4 Numerical results

We now show some numerical results to validate our two-fluid algorithm described in Sect. 3. In all the problems considered below, we carry out the test using the HLLC Riemann solver, the "minmod" limiter in a high-resolution method, and the Courant number 0.9.

Example 4.1 Our first example concerns a model shock–contact interaction problem in one dimension that verifies convergence of our numerical solutions to the weak ones in a multicomponent case. Here the initial condition we use is composed of a stationary air–water interface at $x = 0.6$ m within a 1 meter length domain and a rightward going Mach 1.94 shock wave at $x = 0.5$ m traveling from left to right. The fluid on the right of the interface is an air with the state variables

$$(\rho, \, p, \, \alpha)_R = \left(1.2 \, \text{kg/m}^3, \, 10^5 \, \text{Pa}, \, 0 \right),$$

and the material quantities $\gamma = 1.4$, $b = 2 \times 10^{-3}$ m^3/kg, while the fluid on the left of the interface (ie, on the middle and the pre-shock state) is a water with the state variables

$$(\rho, \, p, \, \alpha)_M = \left(10^3 \, \text{kg/m}^3, \, 10^5 \, \text{Pa}, \, 1 \right).$$

and the material quantities $\gamma = 7$, $\mathcal{B} = 3 \times 10^8$ Pa, $\rho_0 = 10^3$ kg/m^3, $p_0 = 10^5$ Pa. The state behind the shock is taken to be

$$(\rho, \, u, \, p, \, \alpha)_L = \left(1,337.61 \, \text{kg/m}^3, \, 710.525 \, \text{m/s}, \right.$$
$$\left. 2 \times 10^9 \, \text{Pa}, \, 1 \right);$$

see the dashed line shown in Fig. 1 for illustration. We note that in this instance as the interface is accelerated by a shock wave coming from the heavy-fluid to the light-fluid region, it is known that the resulting wave pattern after the interaction would consist of a transmitted shock wave, an interface, and a reflected rarefaction wave.

A snap shot of the computed solutions for $\rho_1 \alpha$, $\rho - \rho_1 \alpha$, u, and p is shown in Fig. 1 at time $t = 200 \, \mu$s, where we solve the problem using the high-resolution method with 400 mesh points. Observing the displayed profiles, we see clearly the good behavior of the computed air-water interface and also the shock and rarefaction waves as in comparison with the exact solution.
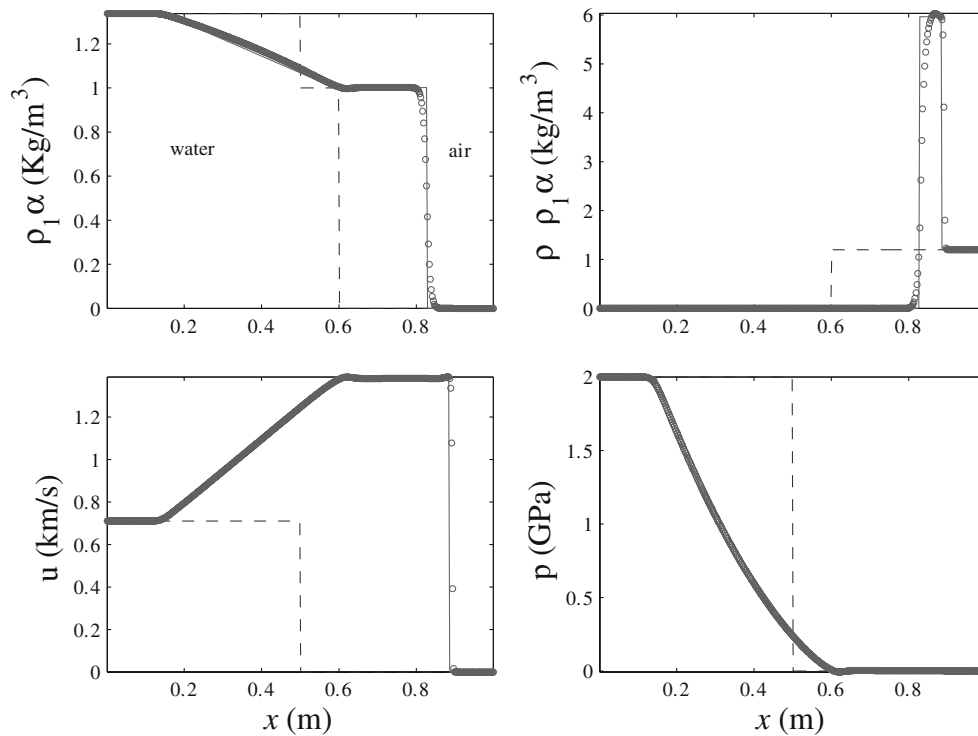
Fig. 1 High-resolution results for a model one-dimensional shock-contact interaction problem at time $t = 200$ μs. The *solid line* is the exact solution and the *points* show the computed solu-

tion with 400 mesh points. The *dashed line* in each subplot is the initial condition at time $t = 0$

Example 4.2 We are next concerned with a radially symmetric problem where the computed solutions in two space dimensions can be compared to the one-dimensional results for numerical validation. In this test, we use the following two-phase (gas–liquid) flow data for experiments in which, in the gas phase, the state variables are

$$(\rho, p, \alpha) = \left(1,250 \text{ kg/m}^3, \ 10^9 \text{ Pa}, \ 1\right)$$

and

$$(\rho, p, \alpha) = \left(1.2 \text{ kg/m}^3, \ 10^5 \text{ Pa}, \ 1\right)$$

if $r < r_1$ and $r > r_2$, respectively, while in the liquid phase they are

$$(\rho, p, \alpha) = \left(10^3 \text{ kg/m}^3, \ 10^5 \text{ Pa}, \ 0\right)$$

if $r_1 < r \le r_2$, where $r = \sqrt{x^2 + y^2}$, $r_1 = 0.2$ m, and $r_2 = 0.7$ m. Here the material quantities of the fluid are taken the same as before, with the exception that a smaller value of the constant for the excluded volume, $b = 10^{-4}$ m^3/kg, is used for the gas.

We note that for this problem all the fluid components are in a resting state initially with zero total velocity, but due to the pressure difference between the fluids at $r = r_1$, breaking of the inner circular membrane occurs instantaneously, yielding an outward-going shock

wave in liquid, an inward-going rarefaction wave in gas, and a material interface lying in between that separates the gas and liquid. As times go along, the inward-going wave would be reflected from the geometric center that generates a new outward-going wave and induces the subsequent interaction of waves. At a somewhat later time, the outward-going shock wave would be collided with the outer gas–liquid interface at $r = r_2$ that results in a wave pattern consisting of a transmitted shock wave, an interface, and a reflected rarefaction wave. Because of the symmetry of the solution, for simplicity, we only take a quarter of the unit square and make use of the line of symmetry boundary conditions to the bottom and the left sides during the computations.

Figures 2 and 3 show numerical results for the total density, radial velocity (defined as $\bar{u} = \sqrt{u^2 + v^2}$), and pressure, at three stopping times, $t = 120$, 240, and 450 μs, where the test has been carried out using a 200×200 grid with the high-resolution method. Clearly, from the contour plots shown in Fig. 2, we observe good resolution of the solution structure (i.e., both the shock and interface remain circular and appear to be very well located) after the breaking of the membrane and also the interaction of the shock and the outer interface.

The scatter plots shown in Fig. 3 provide the validation of our two-dimensional results as in comparison with the

Fig. 2 High-resolution
results for a two-phase
radially symmetric problem.
Contour plots for the total
density, radial velocity, and
pressure are shown at three
different times $t = 120, 240$,
and $450 \,\mu$s, using a 200×200
grid. The dashed line shown
in the graph is the
approximate location of the
gas–liquid interface
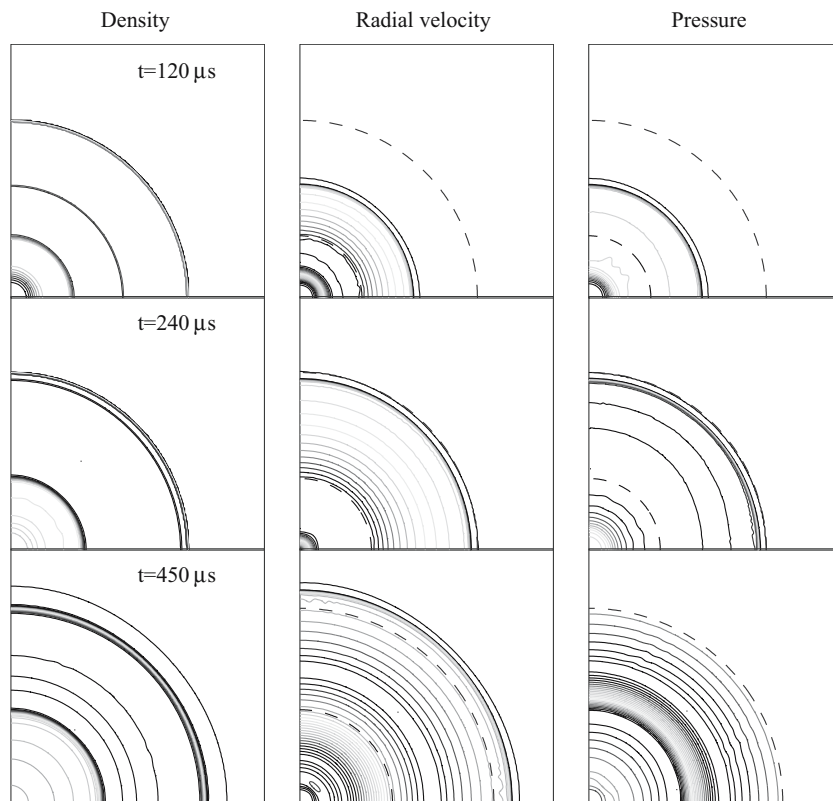
"true" solution obtained from solving the one-dimensional model with appropriate source terms for radial symmetry, using the high-resolution method with 1000 mesh points in a unit length domain. In other words, for the equation, we have a modified-version of the model (27) in one dimension as

$$\frac{\partial q}{\partial t} + f\left(\frac{\partial}{\partial r}, q\right) = \psi(q) \qquad (36)$$

with f a vector-value function defined by

$$f = \left[\frac{\partial}{\partial r}(\rho u), \ \frac{\partial}{\partial r}\left(\rho u^2 + p\right), \ \frac{\partial}{\partial r}(\rho E u + p u),\right.$$
$$\left.\frac{\partial}{\partial r}(\rho_1 \alpha u), \ u\frac{\partial \alpha}{\partial r}\right]^{\mathrm{T}},$$

and ψ the source term derived directly from the geometric simplification of a multidimensional flow to a one-dimensional one,

$$\psi = -\frac{\iota}{r}\left(\rho u, \ \rho u^2, \ \rho E u + p u, \ \rho_1 \alpha u, \ 0\right)^{\mathrm{T}}.$$

Note that in the case of a 2D radially or 3D spherically symmetric flow, we use the quantity $\iota = 1$ or 2, respectively; u now denotes the particle velocity in the r-(radial) direction. We use a Strang-type time splitting procedure [38] to deal with the geometric sources of (36) in a high-resolution manner during the run. From the figure, it is clear that our results agree quite well with the "true" solutions at all the selected times and also

free of wrong fluctuations in the pressure near the inner and outer interfaces before and after the interactions of rarefaction and shock waves.

Example 4.3 To show how our algorithm performs on shock waves in a more general two-dimensional geometry, we are interested in the simulation of a shock-induced collapse of a cylindrical air cavity in water studied by Bourne and Field [7] experimentally and Ball etal [5] numerically. We setup the problem by introducing a stationary air cavity of radius $r_0 = 3$ mm located at $(x_0, y_0) = (6, 0)$ mm and also a planarly rightward-going shock wave in water at $x = 1$ mm approaching toward the cavity on the left. Similar to the initial condition employed in Example 4.1, inside the air bubble, we use the data on the state R as before, while outside the air bubble (the fluid is water), we use the data on the states M and L, when they are in the pre-shock and post-shock regions, respectively. Here, in carrying out the computations below, we take a shock tube of size $[0, 15] \times [0, 6]$ mm^2 and use the solid wall boundary condition on the bottom side and the non-reflecting boundary condition on the remaining sides.

Figures 4 shows the Schlieren image of the results for the density and pressure at ten different times $t = i \times 0.4 \,\mu$s, for $i = 1, 2, \ldots, 10$ (measured relative to a time when the incident shock wave first hits the upstream wall of the air cavity), using the same high-resolution method
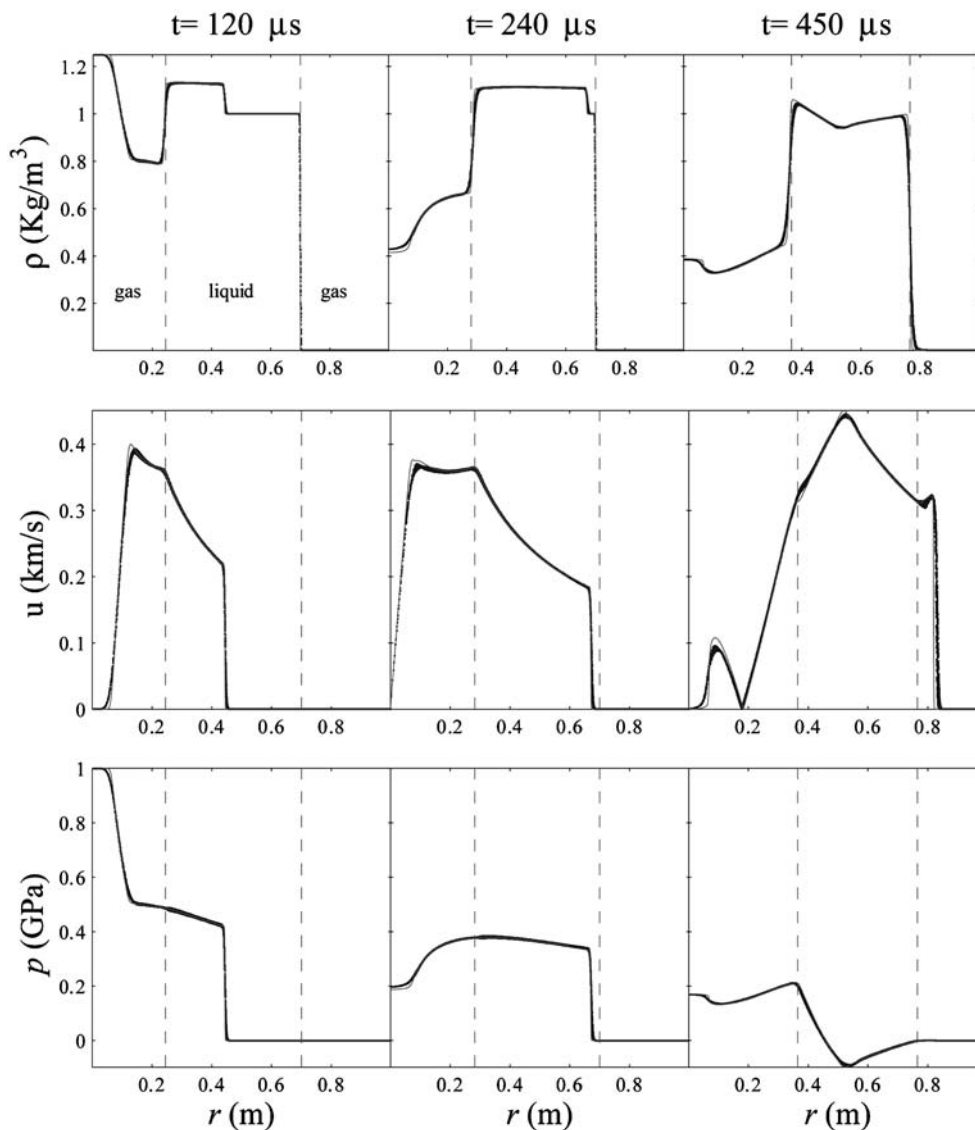
Fig. 3 Scatter plots of the results for the run shown in Fig. 2. The *solid line is the* "true" solution obtained from solving the one-dimensional model with appropriate source terms for the radial symmetry using the high-resolution method and 1,000 mesh points. The *dotted points* are the two-dimensional result. The *dashed line* is the approximate location of the gas-liquid interface

as in the previous example and a $1,500 \times 600$ grid. From the figure, it is easy to see that after the passage of the shock to the cavity, the upstream wall begins to spall across the cavity, yielding a refracted air shock traveling within it at the speed $V_r \approx 2.231$ km/s until its first reflection on the far cavity wall at the time $t \approx 2.647 \mu$s (see the comments given below on how to obtain these numerical values). Noticing that this upstream cavity wall would involute eventually to form a jet which subsequently crosses the cavity and sends an intense blast wave out into the surrounding liquid upon impacting with the far cavity wall.

Following from [7], the time from the initial impingement of the shock on the upstream wall to the impact of the jet on the downstream wall is referred to as the collapsed time t_c. In the current case, we find $t_c \approx 2.787 \mu$s, while the experimental result shown in [7] is about $t_c = 1.8 \pm 0.2 \mu$s for an air cavity of the same diameter in gelatin. At a later stage of the collapse, highly compressed air would be trapped in a lobe-like region (see the plots at times $t = 3.6$ and 4μs), where high pressure and also high temperature are concentrated on. It should be mentioned that this lobe-like region is the place where light emission was observed in an experimental work of Bourne and Field [7]. As the time goes along, complex multiple reflection of waves would continue to happen. The cross-section of the results for the same run along the bottom boundary is drawn in Fig. 5 giving some quantitative information about the density and pressure at the selected times. As far as the global
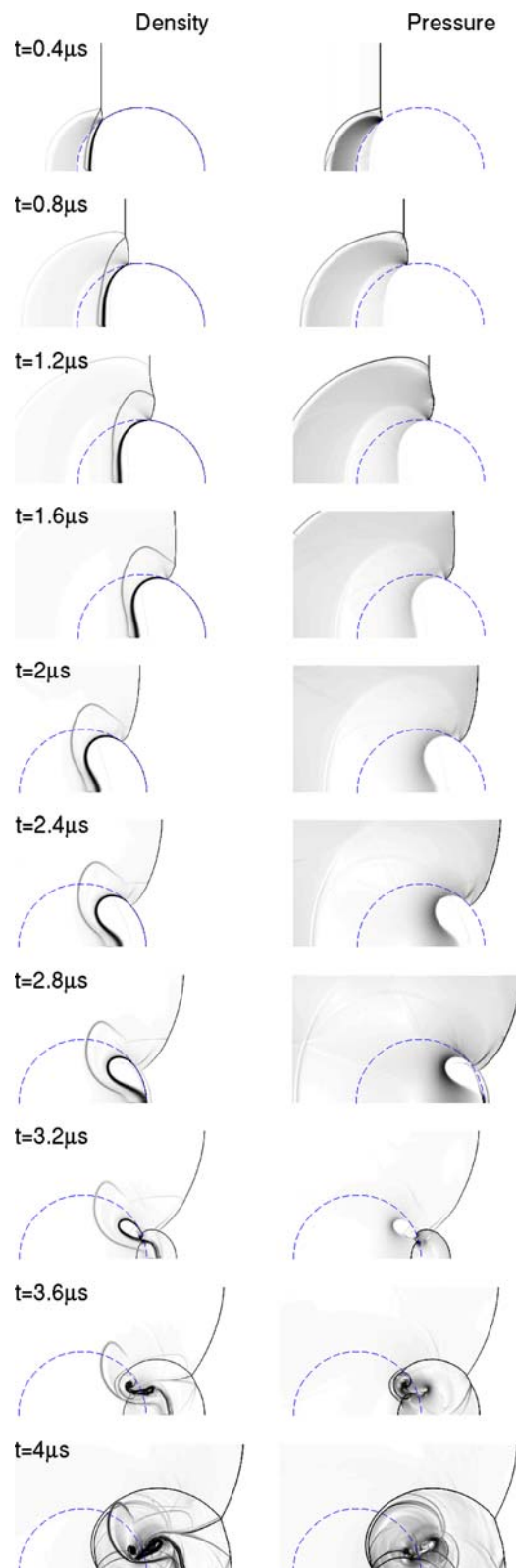
Fig. 4 Two-dimensional results for a planar shock wave in water over a cylindrical air cavity. Schlieren-type image for the density and pressure are shown at ten different times $t = i \times 0.4\mu$s, for $i = 1, 2, \ldots, 10$, where a $1,500 \times 600$ grid was used in the computation. The *dashed line* is the initial location of the air–water interface

wave structure of the solution is concerned the results presented here are reasonable one as compared to the one appearing in Ball et al. [5], where a Free-Lagrange method was employed to solve a similar problem but with a γ-law gas for the air and an incident shock pressure 1.9 GPa; the grid resolution employed in there is 5×10^4 which is 18 times coarser than the grid size used here.

To get a further assessment of the key characteristics of the solutions in the problem, in Fig. 6, we report a diagnosis of the space-time locations of the incident shock wave, the upstream cavity wall, the downstream cavity wall, the first refracted shock wave, and the jet, where we again use a $1,500 \times 600$ grid and the same numerical method as before. With that, it is a common practice (cf. [22,28]) to perform a linear least-squares fit of these trajectories separately and take the slope of the respective line as one measure of the speed of V_s, V_u, V_d, V_r, and V_j, in the order mentioned. Here, at some sample times, we obtain the positions of the incident and refracted shocks by checking the jumps in the pressure to see whether there are greater than a prescribed tolerance, say $\varepsilon_p = (p_L - p_M)/10$, at the horizontal sections of 0.01 mm below the top boundary and the axis of symmetry, respectively. As to the positions of the other features, we check the volume fractions to see if the are close to 0.5 at the axis of symmetry, with the exception that, for the upstream wall, we use a section at a height 1.2 mm above the axis when time $t \geq 1.5\mu$s.

For this air-cavity collapse problem in water, it is of great interest to see how the collapse time t_c as well as the velocity of the jet are varied as we change the magnitude of the incident shock pressure. Here we carry out one such computation with the set of pressure $p_L = i \times 0.5$ GPa, for $i = 1, 2, \ldots, 8$, and show the result in Table 1, observing a monotonic decreasing and so increasing of the collapsed time and jet velocity, respectively, as the incident shock pressure increases; this is consistent with the findings shown in Table 1 of [7]. Figure 7 is the graph about the jet velocity together with the Hugoniot locus for water with the same pre-shock condition as before. Notice that the Hugoniot now divides the graph into two parts where in the lower part the jet velocity is less than the shock velocity and so the incident shock crosses the cavity ahead of the jet, while in the upper part the jet arrives at the downstream cavity wall first and may send out a shock in the material downstream of the cavity ahead of the incident shock. In case the incident shock pressure is in close neighborhood of 3.5 GPa, the speed of the incident shock would be in the proximity to that of the jet. A figure of this kind has also been displayed in the experimental work of Bourne and Field [7], giving some
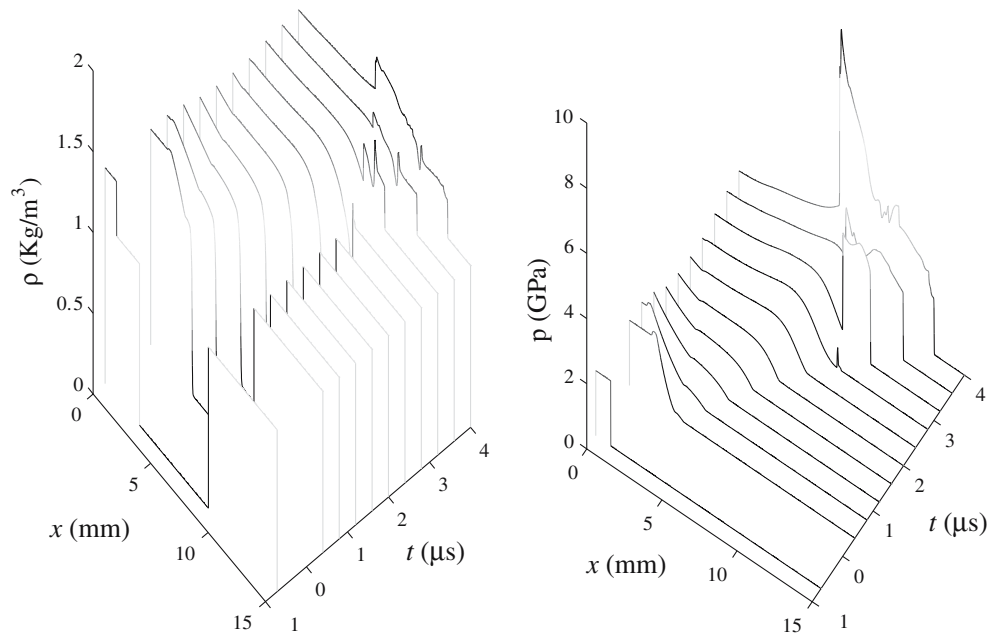
Fig. 5 Cross-sectional plots of the results for the run shown in Fig. 4 along the bottom boundary

Fig. 6 Space-time locations of the incident shock wave, the upstream cavity wall, the downstream cavity wall, the first refracted shock wave, and the jet for the run shown in Fig. 4. These trajectories can be used to estimate the speeds such as V_s, V_u, V_d, V_r, and V_j in the order mentioned above
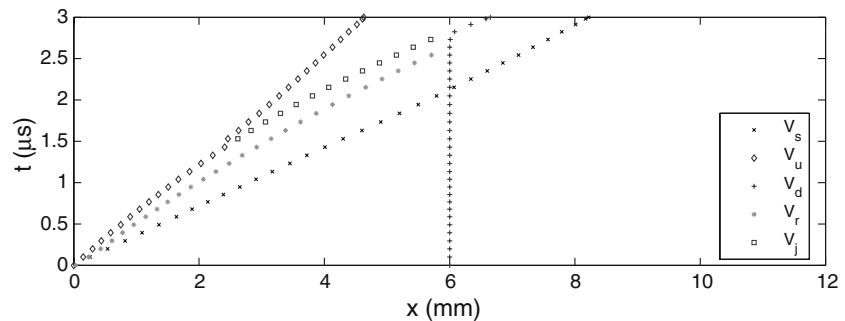

Table 1 Data summarizing solutions of a shock-induced air cavity problem for the particle velocity, jet velocity, and collapsed time, at incident shock pressures $p_L = i \times 0.5$ GPa, for $i = 1, 2, \ldots, 8$

Shock pressure (GPa)	Particle velocity (km/s)	Jet velocity (km/s)	Collapsed time (μs)
0.5	0.256	1.309	6.091
1.0	0.435	1.817	4.119
1.5	0.582	2.191	3.290
2.0	0.711	2.572	2.787
2.5	0.826	2.729	2.487
3.0	0.933	3.064	2.258
3.5	1.032	3.350	2.072
4.0	1.125	3.625	1.952

indication of the sensible behavior of the solutions on the computed jet velocity. It should be remarked that Bagabir and Drikakis [4] have done a similar numerical study, but used the Mach number as the basic parameter for a shock wave in air over a cylindrical helium cavity.

Finally, Fig. 8 shows numerical results for a study of the time history of the volume fraction of the air cavity at four different incident shock pressures $p_L = 1, 2, 3,$ and 4 GPa. As a close look at the data for each of the displayed volume fraction, we may find a time interval during which α falls from 0.8 to 0.1 at almost a linear rate. Consider the case when $P_L = 2$ GPa, for example, the time interval for that to occur is $t \in [0.862, 2.933]\mu$s. Our results also show that not long after the collapsed time the volume continues to decline, but at a somewhat reduced rate which is compatible with many results shown for shock-driven collapse of cylindrical cavities in fluid dynamical problems (cf. [5,7,12]). A detailed study of this problem for a spherical air cavity case in three dimensions will be reported elsewhere.

5 Conclusions

We have described an Eulerian interface-capturing approach for a hybrid barotropic and non-barotropic two-fluid flow problem in more than one space dimension.

Fig. 7 The variation of the jet velocity, denoted by V_j for the shock-induced air-cavity problem, with incident shock pressures $p_L = i \times 0.5$ GPa, for $i = 1, 2, \ldots, 8$. The *solid line* shown in the graph is the Hugoniot locus for water with same pre-shock condition as in Fig. 4, and the *dotted points* are the numerical results
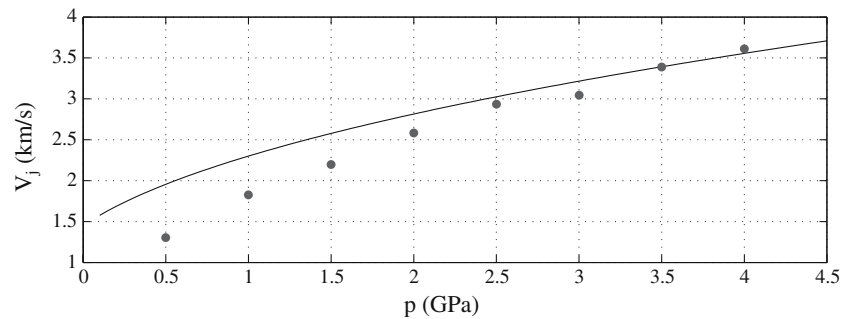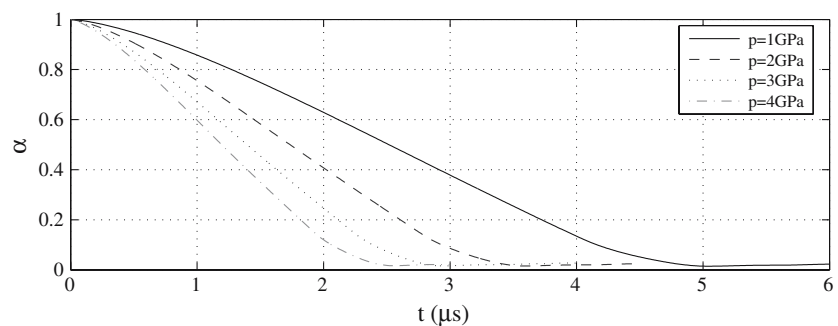

Fig. 8 The time history of the volume fraction of the air cavity at four different incident shock pressures $p_L = 1, 2, 3,$ and 4 GPa

The algorithm uses a volume-fraction formulation of the model equations together with an extended equation of state that is devised to ensure a consistent approximation of the energy equation near the numerical-induced smeared material interfaces and an easy computation of the pressure from the equation of state. A high-order Godunov method based on the wave-propagation viewpoint is employed to solve the proposed model system with the dimensional-splitting technique included in the method for multidimensional problems. Numerical results presented in this paper demonstrate clearly the feasibility of the approach for a reasonable class of two-fluid problems with the thermodynamic property of the barotropic and non-barotropic fluid components characterized by the Tait and Noble–Abel equations of state, respectively.

References

1. Abgrall, R.: How to prevent pressure oscillations in multi-component flow calculations: a quasi conservative approach. J. Comput. Phys. **125**, 150–160 (1996)
2. Abgrall, R., Nkonga, B., Saurel, R.: Efficient numerical approximation of compressible multi-material flow for unstructured meshes. Comput. Fluids **32**, 571–605 (2003)
3. Allaire, G., Clerc, S., Kokh, S.: A five-equation model for the simulation of interface between compressible fluids. J. Comput. Phys. **181**, 577–616 (2002)
4. Bagabir, A., Drikakis, D.: Mach number effects on shock–bubble interaction. Shock Waves **11**, 209–218 (2001)
5. Ball, G.J., Howell, B.P., Leighton, T.G., Schofield, M.J.: Shock-induced collapse of a cylindrical air cavity in water: a free-Lagrange simulation. Shock Waves **10**, 265–276 (2000)
6. Batten, P., Clarke, N., Lambert, C., Causon, D.: On the choice of wave speeds for the HLLC Riemann solvers. SIAM J. Sci. Comput. **18**, 1553–1570 (1997)
7. Bourne, N.K., Field, J.E.: Shock-induced collapse of single cavities in liquid. J. Fluid Mech. **244**, 225–240 (1992)
8. Dear, J.P., Field, J.E.: A study of the collapse of arrays of cavities. J. Fluid Mech. **190**, 409–425 (1988)
9. Fedkiw, R.P., Aslam, T., Merriman, B., Osher, S.: A non-oscillatory Eulerian approach to interfaces in multimaterial flows (the ghost fluid method). J. Comput. Phys. **152**, 457–492 (1999)
10. Fermi, E.: Thermodynamics. Dover, New York (1956)
11. Godlewski, E., Raviart, P.A.: Numerical Approximation of hyperbolic systems of conservation laws. Applied Mathematical Science. Springer, 118 Berlin Heldelverg New York (1996)
12. Haas, J.F., Sturtevant, B.: Interaction of weak shock waves with cylindrical and spherical gas inhomogeneities. J. Fluid Mech. **181**, 41–76 (1987)
13. Harten, A., Lax, P.D., van Leer, B.: On upstream differencing and Godunov-type schemes for hyperbolic conservation laws. SIAM Rev. **25**, 35–61 (1983)
14. Karni, S.: Multicomponent flow calculations by a consistent primitive algorithm. J. Comput. Phys. **112**, 31–43 (1994)
15. Koren, B., Lewis, M.R., van Brummelen, E.H., van Leer, B.: Riemann-problem and level-set approaches for homentropic two-fluid flow computations. J. Comput. Phys. **185**, 654–674 (2002)
16. Langseth, J.O., LeVeque, R.J.: A wave propagation method for three-dimensional hyperbolic conservation laws. J. Comput. Phys. **165**, 126–166 (2000)
17. LeVeque, R.J.: High resolution finite volume methods on arbitrary grids via wave propagation. J. Comput. Phys. **78**, 36–63 (1988)
18. LeVeque, R.J.: Wave propagation algorithms for multi-dimensional hyperbolic systems. J. Comput. Phys. **131**, 327–353 (1997)

19. LeVeque, R.J.: Finite Volume Methods for Hyperbolic Problems. Cambridge University Press, Cambridge (2002)
20. Lide, D.R.: Handbook of Chemistry and Physics, 76th edn. CRC Press, Boca Raton (1996)
21. Luo, H., Baum, J.D., Löhner, R.: On the computation of multi-material flows using ALE formulation. J. Comput. Phys. **194**, 304–328 (2004)
22. Marquina, A., Mulet, P.: A flux-split algorithm applied to conservative models for multicomponent compressible flows. J. Comput. Phys. **185**, 120–138 (2003)
23. Marsh, S.P.: LASL Shock Hugoniot Data. University of California Press, Berkeley (1980)
24. Massoni, J., Saurel, R., Nkonga, B., Abgrall, R.: Proposition de méthodes et modèles eulériens pour les problèms à interfaces entre fluides compressibles en présence de transfert de chaleur(in French). Int. J. Heat Mass Transfer **45**, 1287–1307 (2002)
25. Murnaghan, F.D.: Finite Deformation of an Elastic Solid. Wiley, New York (1951)
26. Murrone, A., Guillard, H.: A five reduced equation model for compressible two-phase flow problems. J. Comput. Phys. **202**, 664–698 (2004)
27. Nagoya, H., Obara, T., Takayama, K.: Underwater shock wave propagation and focusing in inhomogeneous media. In: Brun, R., et al. (eds.) Proceedings of 19th International Symposium on Shock Waves, Marseille. pp. 439–444 Springer Berlin, Heidelverg New York (1995)
28. Quirk, J.J., Karni, S.: On the dynamics of a shock-bubble interaction. J. Fluid Mech. **318**, 129–163 (1996)
29. Roe, P.L.: Fluctuations and signals — A framework for numerical evolution problems. In: Morton, K.W., et al. (eds.) Numerical Methods for Fluid Dynamics, pp. 219–257 Academic New York, pp. 219–257 (1982)
30. Roe, P.L.: Upwind schemes using various formulations of the Euler equations. In: Angrand, F., et al. (eds.) Numerical Methods for the Euler Equations of Fluid Dynamics, pp. 14–31. SIAM, Philadelphia (1985)
31. Saurel, R., Abgrall, R.: A simple method for compressible multifluid flows. SIAM J. Sci. Comput. **21**, 1115–1145 (1999)
32. Shyue, K.M.: An efficient shock-capturing algorithm for compressible multicomponent problems. J. Comput. Phys. **142**, 208–242 (1998)
33. Shyue, K.M.: A fluid-mixture type algorithm for compressible multicomponent flow with van der Waals equation of state. J. Comput. Phys. **156**, 43–88 (1999)
34. Shyue, K.M.: A volume-of-fluid type algorithm for compressible two-phase flows. In: Fey, M., et al. (eds.) Hyperbolic Problems: Theory, Numerics, Applications. Birkhäuser-Verlag, International. Series of Numerical Mathematics, vol. 130, pp. 895–904. Birkhäuser, Germany (1999)
35. Shyue, K.M.: A fluid-mixture type algorithm for compressible multicomponent flow with Mie-Grüneisen equation of state. J. Comput. Phys. **171**, 678–707 (2001)
36. Shyue, K.M.: A fluid-mixture type algorithm for barotropic two-fluid flow problems. J. Comput. Phys. **200**, 718–748 (2004)
37. Smith, R.W.: AUSM (ALE): a geometrically conservative arbitrary Lagrangian–Eulerian flux splitting scheme. J. Comput. Phys. **150**, 268–286 (1999)
38. Strang, G.: On the construction and comparison of difference schemes. SIAM J. Numer. Anal. **5**, 506–517 (1968)
39. Sweby, P.K.: High resolution schemes using flux limiters for hyperbolic conservation laws. SIAM J. Numer Anal. **21**, 995–1011 (1984)
40. Toro, E.F.: A fast Riemann solver with constant covolume applied to the random choice method. Int. J. Numer. Methods in Fluids **9**, 1145–1164 (1989)
41. Toro, E.F.: Riemann Solvers and Numerical Methods for Fluid Dynamics: A Practical Introduction, 2nd Edn.. Springer-Berlin Heidelberg Nwe York (1999)
42. Toro, E.F., Spruce, M., Speares, W.: Restoration of the contact surface in the HLL-Riemann solver. Shock Waves **4**, 25–34 (1994)
43. van Brummelen, E.H., Koren, B.: A pressure-invariant conservative Godunov-type method for barotropic two-fluid flows. J. Comput. Phys. **185**, 289–308 (2003)
44. Wardlaw, A.B.,Jr., Mair, H.U.: Spherical solutions of an underwater explosion bubble. Shock Vibr. **5**, 89–102 (1998)
45. Yamada, K., Nagoya, H., Takayama, K.: Shock wave reflection and refraction over a two-fluid interface. In: Brun, R., et al. (eds.) Proceedings of 19th International Symphosium on Shock Waves, MarseilleSpringer, Berlin Aeidelberg New York Berlin, pp. 299–304 (1995)